Title

Enantioselective Recognition of Ammonium Carbamates in a Chiral Metal—Organic Framework

Journal

Journal of the American Chemical Society, 139(44)

ISSN

0002-7863

Authors

Martell, Jeffrey D

Zasada, Leo B

Forse, Alexander C

et al.

Publication Date

2017-11-08

DOI

10.1021/jacs.7b09983

Peer reviewed

JACS
JOURNAL OF THE AMERICAN CHEMICAL SOCIETY
Article
Cite This: J. Am. Chem. Soc. 2017, 139, 16000-16012
pubs.acs.org/JACS

Enantioselective Recognition of Ammonium Carbamates in a Chiral Metal−Organic Framework

Jeffrey D. Martell,[†,‡] Leo B. Porter-Zasada,[†] Alexander C. Forse,[†,§,∥] Rebecca L. Siegelman,[†] Miguel I. Gonzalez,[†] Julia Oktawiec,[†] Tomče Runčevski,[†,⊥] Jiawei Xu,[#] Monika Srebro-Hooper,[▽] Phillip J. Milner,[†] Kristen A. Colwell,[§] Jochen Autschbach,[○] Jeffrey A. Reimer,[§,⊥] and Jeffrey R. Long*[,†,§,⊥]

[†]Department of Chemistry, University of California, Berkeley, California 94720, United States
[‡]Miller Institute for Basic Research in Science, University of California, Berkeley, California 94720, United States
[§]Department of Chemical and Biomolecular Engineering, University of California, Berkeley, California 94720, United States
[∥]Berkeley Energy and Climate Institute, University of California, Berkeley, California 94720, United States
[⊥]Materials Sciences Division, Lawrence Berkeley National Laboratory, Berkeley, California 94720, United States
[#]Jasco Corporation, 2967-5 Ishikawa-machi, Hachioji-shi, Tokyo 192-8537, Japan
[▽]Faculty of Chemistry, Jagiellonian University, 30-387 Krakow, Poland
[○]Department of Chemistry, University at Buffalo, State University of New York, Buffalo, New York 14260, United States

Supporting Information

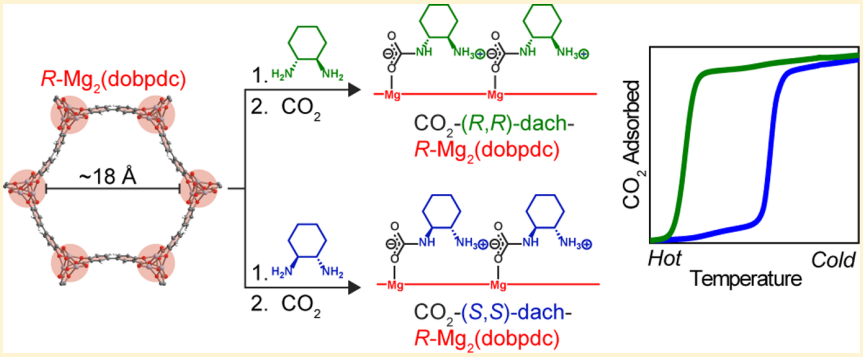

ABSTRACT: Chiral metal−organic frameworks have attracted interest for enantioselective separations and catalysis because of their high crystallinity and pores with tunable shapes, sizes, and chemical environments. Chiral frameworks of the type M_2(dobpdc) (M = Mg, Mn, Fe, Co, Ni, Zn; dobpdc^{4-} = 4,4′-dioxidobiphenyl-3,3′-dicarboxylate) seem particularly promising for potential applications because of their excellent stability, high internal surface areas, and strongly polarizing open metal coordination sites within the channels, but to date these materials have been isolated only in racemic form. Here, we demonstrate that when appended with the chiral diamine *trans*-1,2-diaminocyclohexane (dach), Mg_2(dobpdc) adsorbs carbon dioxide cooperatively to form ammonium carbamate chains, and the thermodynamics of CO_2 capture are strongly influenced by enantioselective interactions within the chiral pores of the framework. We further show that it is possible to access both enantiomers of Mg_2(dobpdc) with high enantiopurity (≥90%) via framework synthesis in the presence of varying quantities of D-panthenol, an inexpensive chiral induction agent. Investigation of dach−M_2(dobpdc) samples following CO_2 adsorption—using single-crystal and powder X-ray diffraction, solid-state nuclear magnetic resonance spectroscopy, and density functional theory calculations—revealed that the ammonium carbamate chains interact extensively with each other and with the chiral M_2(dobpdc) pore walls. Subtle differences in the non-covalent interactions accessible in each diastereomeric phase dramatically impact the thermodynamics of CO_2 adsorption.

INTRODUCTION

The synthesis and separation of enantiopure chiral molecules are extremely important in the pharmaceutical industry because a large percentage of drugs are chiral[1] and individual enantiomers of these drugs must be isolated and tested for efficacy and safety.[2] Both chiral separations and enantioselective catalysis require preferential selection of an individual enantiomer of a guest molecule or transition state within a chiral host. Chiral metal−organic frameworks are promising materials for enantioselective

Received: September 18, 2017
Published: October 9, 2017

DOI: 10.1021/jacs.7b09983
J. Am. Chem. Soc. 2017, 139, 16000−16012

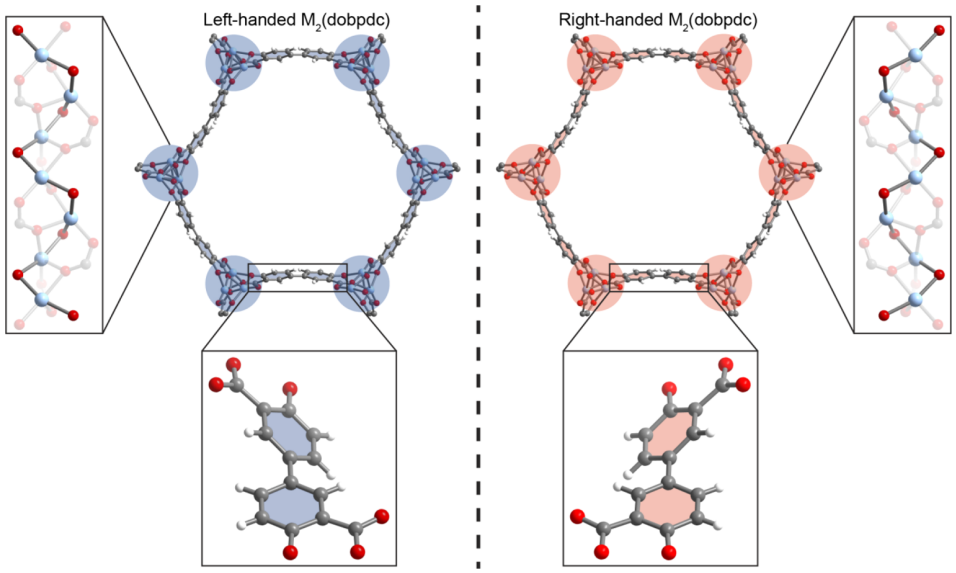

Figure 1. Structures of the left- and right-handed enantiomers of M_2(dobpdc). The chirality of this material arises from the twist of the organic linker (dobpdc^{4-}), which the framework locks into a chiral conformation, and the helices, which form the corners of the 1.8 nm one-dimensional hexagonal channels. The left-handed Mg_2(dobpdc) enantiomer (space group $P3_221$) contains only left-handed helices, and right-handed Mg_2(dobpdc) enantiomer (space group $P3_121$) contains only right-handed helices. After the framework is heated under vacuum, the corners of the hexagon-shaped channels are lined with coordinatively unsaturated metal sites, which are strong binding sites for guest molecules. Light-blue spheres represent M^{2+} cations. Red, gray, and white spheres represent O, C, and H atoms, respectively. The structure depicted in this figure is Zn_2(dobpdc).[21]

recognition because of their highly tunable structures and three-dimensional pores that can be precisely tailored for adsorption of specific guest molecules. Although numerous chiral metal–organic frameworks have been reported and several have been employed for chiral separations[3−7] or enantioselective catalysis,[8−13] their synthesis often requires complex chiral starting materials[7,10,13] that are costly to synthesize and difficult to obtain on a large scale. A promising alternative strategy is to synthesize a chiral framework from less expensive achiral starting materials. Although this approach leads to the formation of a bulk racemic solid containing both left- and right-handed domains, homochirality can sometimes be induced using inexpensive chiral additives during synthesis.[14−18] Nonetheless, it remains challenging to design chiral metal–organic frameworks that can be synthesized on a large scale, exhibit high internal surface area (and thus the potential for a high adsorption capacity), and maintain permanent porosity upon activation. Furthermore, most chiral metal–organic frameworks are not amenable to postsynthetic functionalization, which precludes the possibility of tuning the pore interior for particular applications.

One potentially promising type of chiral metal–organic framework is M_2(dobpdc) (dobpdc^{4-} = 4,4′-dioxidobiphenyl-3,3′-dicarboxylate),[19,20] which is an expanded variant of the well-studied M_2(dobdc) (dobdc^{4-} = 2,5-dioxidobenzene-1,4-dicarboxylate) framework and features ∼18 Å-wide hexagonal channels running along the crystallographic *c* axis (Figure 1).[22] The walls of each hexagonal channel are formed by the dobpdc^{4-} organic linkers, and the corners consist of metal–oxo helices that are formed by coordination of the oxygen donor groups of the linkers to the divalent metal cations. In the as-synthesized material, each metal sits in an octahedral pocket wherein one coordination site, facing into the pore, is occupied by a solvent molecule. This solvent can be removed by heating the material under reduced pressure to yield an activated framework with a high density of open coordination sites available for binding of guest molecules. Alternatively, the solvent molecules can be replaced postsynthetically by other coordinating molecules such as diamines, rendering the interior of this framework highly tunable.[19−21,23,24]

The chirality of the M_2(dobpdc) structure arises from the twisted conformation of the dobpdc^{4-} organic linker and the metal–oxo helices, which are either all left-handed or all right-handed in individual subdomains of the material (Figure 1). This framework is permanently porous upon evacuation of guest solvent molecules and exhibits a high internal surface area (>4000 m^2/g for Mg_2(dobpdc)[21]) and excellent thermal stability. Importantly, Mg_2(dobpdc) can be prepared on multigram[21] to kilogram[25] scales and is synthesized from inexpensive achiral starting materials. Despite these promising attributes, M_2(dobpdc) frameworks have yet to be used in chiral separations because they are racemic in bulk (containing an equal number of left- and right-handed pores). Indeed, to date the frameworks have been employed only for applications involving achiral guests.[19−21,23,24,26−31]

We reasoned that Mg_2(dobpdc) could be evaluated for enantioselective guest recognition by grafting of a chiral diamine followed by characterization of CO_2 adsorption. This approach builds upon our previously reported postsynthetic functionalization of M_2(dobpdc) with diamines, which are tethered to the framework via metal–amine bonds, to produce CO_2 adsorbents that operate via a unique cooperative insertion mechanism.[19−21,23,24] Upon exposure to CO_2, a non-metal-bound amine abstracts a proton from a metal-bound amine, and the metal-bound amine reacts with CO_2 to form a carbamate with its oxyanion coordinated to the metal (Figure 2). The unusual step-shaped adsorption profiles reflect the cooperative mechanism of CO_2 capture, in which ammonium carbamates are ion-paired along the *c* axis of Mg_2(dobpdc) in highly stabilized chains. The thermodynamics of CO_2 adsorption, and thus the position of the step, can be tuned by changing the metal in the framework[20] or the diamine.[21] Importantly, because the pore walls also interact with the ammonium carbamate chains through hydrogen bonds

DOI: 10.1021/jacs.7b09983
J. Am. Chem. Soc. 2017, 139, 16000−16012

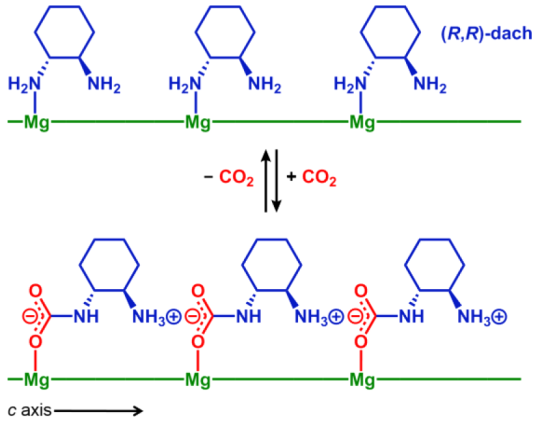

Figure 2. Diamine-appended variants of Mg_2(dobpdc) react cooperatively with gaseous CO_2 to form highly stabilized ammonium carbamate chains along the pore axis (*c* axis) of the material.[20,21] This cooperative reaction gives rise to the unusual step-shaped adsorption exhibited by this material. In particular, (*R*,*R*)-dach was used in this study to test whether the chiral Mg_2(dobpdc) framework can exhibit enantioselectivity in ammonium carbamate formation.

and van der Waals contacts,[21] the chiral channels of Mg_2(dobpdc) could potentially influence the thermodynamics of CO_2 capture by chiral diamines.

Herein we demonstrate that upon grafting enantiomers of the chiral diamine *trans*-1,2-diaminocyclohexane (dach), a high degree of chiral recognition is indeed possible in racemic Mg_2(dobpdc), as evidenced by the distinct thermodynamics of CO_2 adsorption associated with the formation of two diastereomeric ammonium carbamate phases. We further disclose an approach for isolating both enantiomers of Mg_2(dobpdc) with high enantiopurity, facilitating detailed structural and spectroscopic studies of the interactions influencing the stability of the chiral ammonium carbamate chains formed within the framework channels. Intriguingly, subtle differences in hydrophobic packing and hydrogen bonding lead to large differences in the thermodynamics of CO_2 adsorption in the diastereomeric phases.

RESULTS AND DISCUSSION

Enantioselective Recognition of Ammonium Carbamate Chains in Mg_2(dobpdc). The chiral diamine *trans*-1,2-diaminocyclohexane (dach) was selected as a good candidate for grafting to Mg_2(dobpdc) because both of its enantiomers, (*R*,*R*)-dach and (*S*,*S*)-dach, are commercially available and two of its structural analogues, ethylenediamine and (±)-1,2-diaminopropane, have been previously evaluated in this framework.[21,26,28] Following a previously published procedure,[21] soaking methanol-solvated Mg_2(dobpdc) in a 20% (v/v) dach solution yielded (*R*,*R*)-dach–Mg_2(dobpdc) with one dach coordinated per metal site (Figure S10).

In CO_2 isobars measured using thermogravimetric analysis (TGA), (*R*,*R*)-dach–Mg_2(dobpdc) exhibited two sharp adsorption steps at 156 and 120 °C, with each step corresponding to exactly half of the adsorption capacity (Figure 3a). Notably, identical adsorption behavior was observed for (*S*,*S*)-dach–Mg_2(dobpdc) (Figure S1). From these results, we hypothesized that the diastereomeric domains in (*R*,*R*)-dach–Mg_2(dobpdc) exhibit distinct CO_2 adsorption thermodynamics due to enantioselective interactions between the ammonium carbamate chains and the chiral pores of the framework. In contrast,

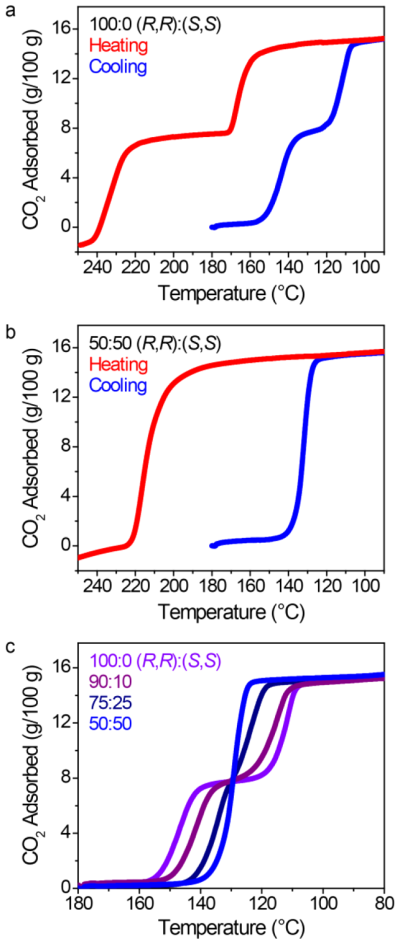

Figure 3. Thermogravimetric analyses of pure CO_2 isobars of Mg_2(dobpdc) functionalized with dach isomers. (a) Adsorption (blue) and desorption (red) isobars for (*R*,*R*)-dach–Mg_2(dobpdc). Identical results were obtained for (*S*,*S*)-dach–Mg_2(dobpdc) (Figure S1). The negative mass above 240 °C can be attributed to diamine volatilization. (b) Adsorption (blue) and desorption (red) isobars for (±)-dach–Mg_2(dobpdc). (c) Adsorption isobars for Mg_2(dobpdc) grafted with varying ratios of (*R*,*R*)- and (*S*,*S*)-dach. A temperature ramp rate of 2 °C/min was employed in collecting all of the data depicted here.

(±)-dach–Mg_2(dobpdc) exhibited a single step at an intermediate temperature between the two steps of (*R*,*R*)-dach–Mg_2(dobpdc) (Figure 3b). Grafting nonracemic mixtures of (*R*,*R*)- and (*S*,*S*)-dach to Mg_2(dobpdc) produced two distinct steps, each corresponding to exactly half of the adsorption capacity, with the separation between the steps decreasing as the (*R*,*R*):(*S*,*S*) ratio approached 1:1 (Figure 3c). Elsewhere we reported that grafting of diamines with bulky alkyl groups to Mg_2(dobpdc) yields two adsorption steps because of steric crowding between ammonium carbamate chains in the *ab* plane;[21,23] however, the two-step adsorption profile observed here cannot be caused by the same mechanism, since (±)-dach—which consists of 50% (*R*,*R*)-dach—exhibits a single adsorption step (Figure 3b).

Desorption isobars for (*R*,*R*)- and (*S*,*S*)-dach–Mg_2(dobpdc) revealed large hysteresis for both the low- and high-temperature steps (~50 and ~90 °C, respectively) (Figures 3a and S1). Using very slow temperature ramp rates decreased the magnitude of the hysteresis but did not completely remove it (Figures S3 and S4). Other 1°,1° variants of ethylenediamine also display large

DOI: 10.1021/jacs.7b09983
J. Am. Chem. Soc. 2017, 139, 16000–16012

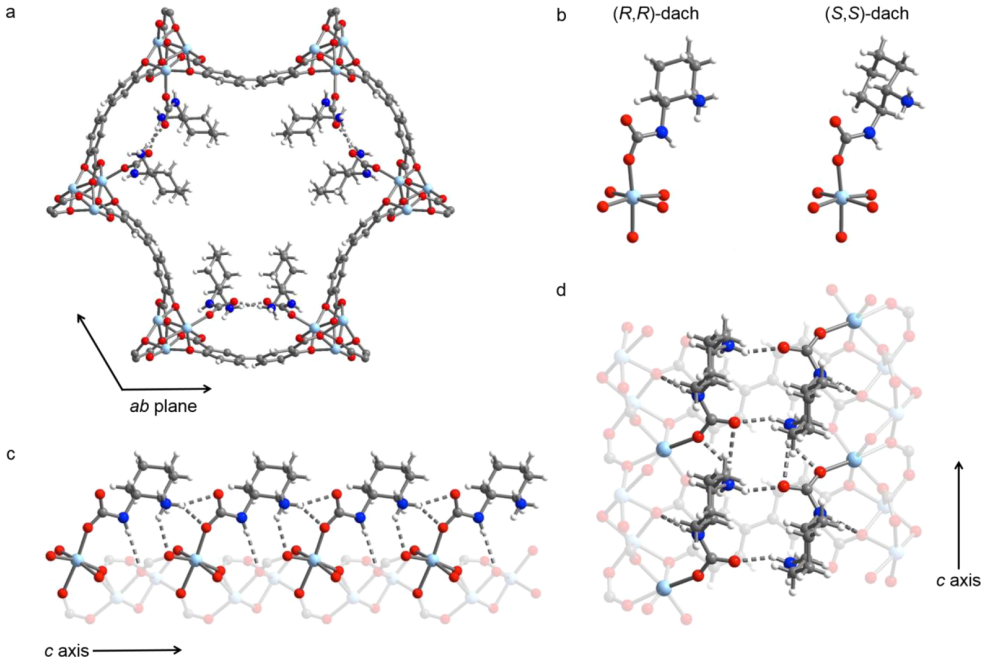

Figure 4. Selected views of the 100 K single-crystal X-ray diffraction structure of CO_2-inserted (±)-dach–Zn_2(dobpdc) depicted in space group $P3_121$ (right-handed framework pores). Light-blue, blue, red, gray, and white spheres represent Zn, N, O, C, and H atoms, respectively. (a) Pore view. Hydrogen bonds between ammonium carbamate chains in the *ab* plane are enabled by framework contraction. Both (*R*,*R*)-and (*S*,*S*)-dach were resolved in the structure, but for clarity, only (*R*,*R*)-dach is shown. (b) Conformations of (*R*,*R*)-and (*S*,*S*)-dach ammonium carbamates, which were both resolved in the structure. The carbamate carbon, nitrogen, and oxygen atoms and the ammonium nitrogen of (*R*,*R*)- and (*S*,*S*)-dach were exactly superimposed in the structure. (c) View of the ammonium carbamate chains along the *c* axis of the material. For clarity, only (*R*,*R*)-dach is shown. (d) View of hydrogen bonding between neighboring ammonium carbamate chains in the *ab* plane. Hydrogen bonding within the chains along the *c* axis is also visible. For clarity, only (*R*,*R*)-dach is shown.

hysteresis,[21,26,28] but the hysteresis displayed by dach–Mg_2(dobpdc) is the largest observed to date, indicating a very large barrier for CO_2 desorption. Differential enthalpies and entropies of CO_2 adsorption for the low- and high-temperature steps of (*R*,*R*)-dach–Mg_2(dobpdc) as well as the single step of (±)-dach–Mg_2(dobpdc) were estimated using an empirical method based on comparison with published diamine variants (Figures S5–S8 and Table S1; see section 1 in the Supporting Information for a detailed description). Compared with previously studied diamine variants, (±)-dach–Mg_2(dobpdc) and (*R*,*R*)-dach–Mg_2(dobpdc) exhibit the highest step temperatures.

To investigate whether enantioselective interactions with the chiral Mg_2(dobpdc) pores are the origin of the two-step adsorption profile in (*R*,*R*)-dach–Mg_2(dobpdc), dach variants were grafted to Mg_2(pc-dobpdc) (pc-dobpdc^{4-} = 3,3′-dioxidobiphenyl-4,4′-dicarboxylate),[23,32] an achiral isomeric framework. Both M_2(pc-dobpdc) and M_2(dobpdc) possess hexagon-shaped channels with diameters of ∼18 Å and contain a 1:1 ratio of left- and right-handed helices in bulk samples (Figures S15 and S16). However, whereas subdomains of Mg_2(dobpdc) contain helices of a single handedness, Mg_2(pc-dobpdc) crystallizes in the achiral space group $R\bar{3}$ with an equal number of alternating left- and right-handed helices within each pore. Furthermore, the two phenyl rings of pc-dobpdc^{4-} are coplanar in the framework, corresponding to an achiral conformation.[23]

Isobars for the adsorption of CO_2 in (*R*,*R*)-dach–Mg_2(pc-dobpdc) and (±)-dach–Mg_2(pc-dobpdc) both exhibit only a single adsorption step (Figures S17–S19). Therefore, the two adsorption steps in (*R*,*R*)-dach–Mg_2(dobpdc) cannot be explained simply by the presence of left- and right-handed metal–oxo helices. Instead, these results suggest that entire chiral channels of Mg_2(dobpdc) influence the thermodynamics of CO_2 capture.

To further understand the interactions responsible for this observed enantioselectivity, we sought to study the structure of the (±)-dach-appended frameworks both before and after CO_2 adsorption. Because we were unable to grow Mg_2(dobpdc) single crystals of sufficient size for X-ray diffraction, we utilized Zn_2(dobpdc) for these experiments. Alkylethylenediamine-appended Zn_2(dobpdc) frameworks are isostructural to their Mg counterparts and follow the same CO_2 adsorption mechanism.[21] As expected, like its Mg congener, (*R*,*R*)-dach–Zn_2(dobpdc) exhibited two CO_2 desorption steps and large hysteresis upon desorption (Figure S23). Since all single crystals of Zn_2(dobpdc) were found to be racemically twinned, containing left- and right-handed subdomains, grafting of enantiopure dach would create diastereomeric subdomains with a potentially unsolvable diffraction pattern. In contrast, the enantiomeric subdomains of Zn_2(dobpdc) remained enantiomeric after grafting of (±)-dach, leading to a solvable diffraction pattern.

The crystal structure of (±)-dach–Zn_2(dobpdc) displayed well-resolved density for the base framework, with unit cell parameters ($a = b = 21.4931(13)$ Å, $c = 6.6895(5)$ Å) similar to those of the framework solvated by dimethylacetamide ($a = b = 21.526(4)$ Å, $c = 6.7042(15)$ Å).[21] However, the diamines were highly disordered in the structure, even at 100 K, and no clear conformers could be resolved.

In contrast, upon CO_2 dosing, well-defined conformers were resolved for the ammonium carbamate chains, with (*R*,*R*)- and

DOI: 10.1021/jacs.7b09983
J. Am. Chem. Soc. 2017, 139, 16000–16012

(*S*,*S*)-dach present in approximately a 1:1 ratio (Figure 4). In the crystal structure, each ammonium carbamate unit is hydrogen-bonded to its neighbor along the *c* axis to form highly stabilized chains (Figure 4c), consistent with other diamine-appended variants of Zn_2(dobpdc). The N−H group of each carbamate was also observed to hydrogen-bond to carboxylate O atoms in the metal−oxo helix, providing additional stabilization of the CO_2-adsorbed phase. Additional hydrogen bonds between neighboring ammonium carbamate chains in the *ab* plane were also resolved (Figure 4d), a feature that has not been observed in any other ethylenediamine-appended Zn_2(dobpdc) crystal structures to date. This latter interaction was enabled by a unit cell contraction of 4.1% in the *ab* plane ($a = b = 20.6012(7)$ Å) relative to the starting (±)-dach−Zn_2(dobpdc) framework, which brings pairs of ammonium carbamate chains into close proximity, accompanied by a slight expansion along the *c* axis ($c = 6.8939(3)$ Å). We note that the hydrogen bonds in the *ab* plane must be sufficiently strong to induce this otherwise unfavorable distortion and likely contribute to the thermodynamic favorability of CO_2 adsorption in the material.

Importantly, Rietveld refinement of the CO_2-inserted structure of (±)-dach−Mg_2(dobpdc) against the corresponding powder X-ray diffraction pattern confirmed that it is isostructural to CO_2-inserted (±)-dach−Zn_2(dobpdc) (Figure S24). The contraction in the *ab* plane observed for the Zn structure upon CO_2 dosing is also consistent with powder X-ray diffraction data obtained for (*R*,*R*)-dach−Mg_2(dobpdc) and several other 1°,1°-diamine-grafted Mg_2(dobpdc) variants (Figure S13).[26,28] We note that the large hysteresis observed for (±)-dach−Mg_2(dobpdc) and other 1°,1°-diamine-appended variants[21] may arise from the substantial unit cell contraction and/or formation of stabilizing hydrogen bonds in the *ab* plane upon CO_2 adsorption, leading to a large activation barrier for the collective phase transition.[33]

The CO_2-inserted crystal structure offers insight into why grafting of varying mixtures of (*R*,*R*)- and (*S*,*S*)-dach yielded two distinct CO_2 adsorption steps with tunable positions (Figure 3c). In this structure, the ammonium nitrogen, two carbons from the cyclohexane ring, and all of the carbamate atoms of (*R*,*R*)-dach can be superimposed with the corresponding atoms of (*S*,*S*)-dach (Figure 4b). The structure suggests that the (*R*,*R*)- and (*S*,*S*)-dach enantiomers are distributed homogeneously throughout the framework and capture CO_2 cooperatively to form mixed-stereochemistry ammonium carbamate chains with intermediate stability. Consistent with this analysis, it was found that various combinations of 1°,1°-ethylenediamine analogues yielded a tunable step of intermediate temperature (Figures S20−S22 and Table S2). These results suggest that when enriched with (*R*,*R*)-dach, the corresponding ammonium carbamate chains interact more favorably with one enantiomer of Mg_2(dobpdc), while (*S*,*S*)-dach-enriched chains interact more favorably with the opposite Mg_2(dobpdc) enantiomer. The enantiomers of Mg_2(dobpdc) interact equivalently with racemic ammonium carbamate chains, accounting for the single CO_2 adsorption step exhibited by (±)-dach−Mg_2(dobpdc).

We note that because the thermodynamics of CO_2 capture can be tuned by varying the (*R*,*R*):(*S*,*S*) ratio of dach in the framework, the conformations of the (*R*,*R*) and (*S*,*S*) ammonium carbamates in (±)-dach−M_2(dobpdc) are not necessarily representative of the structure of enantiopure dach−M_2(dobpdc). To further understand the structural basis for the enantioselective ammonium carbamate recognition by M_2(dobpdc), we deemed it necessary to study the structure of enantiopure ammonium carbamate chains within enantiopure M_2(dobpdc). Because the racemic nature of M_2(dobpdc)—both the Zn single crystals and Mg powder—prevented this structure from being obtained, we sought to prepare enantiopure Mg_2(dobpdc).

Synthesis of Enantiopure Mg_2(dobpdc) by Chiral Induction. In attempting to prepare enantiopure Mg_2(dobpdc), we first sought to establish an assay to characterize the enantiopurity. We considered techniques such as single-crystal X-ray diffraction and solid-state circular dichroism (CD) spectroscopy. The former technique does not indicate bulk chirality, however, and the small size of the Mg_2(dobpdc) single crystals excluded single-crystal X-ray diffraction as a viable method.[21] While enantiomeric materials exhibit opposite signals via solid-state CD spectroscopy,[34] this method cannot quantify enantiopurity unless an enantiopure standard is available.[14] Instead, we devised the following simple assay to characterize Mg_2(dobpdc) enantiopurity: grafting with enantiopure dach followed by collection of CO_2 adsorption isobars. Whereas (±)-Mg_2(dobpdc) exhibited two steps with exactly equal heights, enantio-enriched Mg_2(dobpdc) samples are expected to deviate from this 1:1 ratio. This assay therefore enables quantification of both the Mg_2(dobpdc) enantiopurity and phase purity, since the height and sharpness of the CO_2 adsorption steps are dependent on the purity and porosity of the material. The quantitative nature of this assay could be further validated by solid-state NMR spectroscopy of CO_2-inserted, dach-appended Mg_2(dobpdc) variants, as discussed below.

A chemically diverse selection of commercially available and nontoxic compounds were examined for inducing uniform chirality in Mg_2(dobpdc), including amino acids, inexpensive chiral alcohols, and the previously reported chiral inducing agents camphoric acid and cinchonine (Figure S28).[15,16] Because the mechanism of nucleation for Mg_2(dobpdc) crystals is unknown, it was difficult to predict a priori which additives would induce homochirality without disrupting framework assembly. However, the amino acid L-proline was a particularly attractive candidate because it is an enantioselective organocatalyst,[35] can induce typically achiral MOF-5 to distort into a semistable chiral structure,[36] and can facilitate the growth of large zirconium-based metal−organic framework crystals.[37]

The synthesis of Mg_2(dobpdc) was initially carried out in the presence of each chiral reagent with an additive:H_4dobpdc molar ratio of 3:1, which was previously employed successfully for chiral induction of a metal−organic framework.[15] The enantiopurity and quality of each resulting Mg_2(dobpdc) sample was assessed via examination of the sharpness of the CO_2 adsorption steps and quantitation of the combined step heights (Figures S29−S37). The majority of the additives caused detectable chiral induction of Mg_2(dobpdc), and for samples displaying chiral induction, grafting of (*R*,*R*)- and (*S*,*S*)-dach yielded exactly opposite high- and low-temperature CO_2 adsorption step behaviors. Namely, high- and low-temperature steps dominated for (*R*,*R*)- and (*S*,*S*)-dach-appended frameworks, respectively, confirming enrichment of one Mg_2(dobpdc) enantiomer (Figure S32). Taking into account both the extent of chiral induction and framework quality, we found the optimal additives to be L-proline and D-panthenol (an inexpensive, industrially produced provitamin derivative of vitamin B_5 and an ingredient in moisturizers and lotions[38]).

Hence, we focused our remaining investigations on frameworks prepared in the presence of these compounds. For example, when the synthesis of Mg_2(dobpdc) was carried out in

DOI: 10.1021/jacs.7b09983
J. Am. Chem. Soc. 2017, 139, 16000−16012

the presence of 5 molar equiv of L-proline (relative to H_4dobpdc), it was possible to optimize the framework enantiomeric purity to 90% (Figure S37). As expected, L- and D-proline yielded opposite enantiomers of Mg_2(dobpdc), and synthesis in the presence of (±)-proline yielded (±)-Mg_2(dobpdc) (Figure S37). Adding ≥10 equiv of proline in the reaction dramatically decreased the Mg_2(dobpdc) yield, while in the presence of 20 equiv of proline, no Mg_2(dobpdc) was formed even after 30 days.

The enantiopurity of Mg_2(dobpdc) could be further optimized by carrying out the synthesis in the presence of D-panthenol (Figure 5a), which is completely miscible with *N*,*N*-dimethylformamide (DMF) and methanol and therefore could be added at very high concentrations. The optimized sample of Mg_2(dobpdc), to which we refer as *R*-Mg_2(dobpdc), could be prepared by combining $Mg(NO_3)_2$ and H_4dobpdc in a 1.3:1 ratio in a 37:31:32 (w/w/w) methanol/DMF/D-panthenol mixture (with concentrations of ~50 and ~37 mM for $Mg(NO_3)_2$ and H_4dobpdc, respectively). Following synthesis and standard washing procedures, no detectable D-panthenol remained in the framework, as determined by ^{1}H NMR spectroscopy carried out on a sample of the digested material (Figures S44–46). When appended with (*R*,*R*)-dach, the *R*-Mg_2(dobpdc) framework exhibited a single, predominant high-temperature step in its CO_2 adsorption isobar, with a quantity of adsorbed CO_2 that accounted for ~95% of its total capacity, indicating ~95% enantiopurity (Figures 5b and S38). The compound (*R*,*R*)-dach–*R*-Mg_2(dobpdc) further displayed sharp CO_2 adsorption steps and high overall CO_2 capacity, equal to that of (±)-Mg_2(dobpdc), indicating excellent sample quality.

Unexpectedly, the opposite enantiomer of Mg_2(dobpdc) could be obtained using the same solvent system and $Mg(NO_3)_2$:H_4dobpdc ratio, but with a 5-fold increase in the concentrations of both $Mg(NO_3)_2$ and H_4dobpdc (Figure 5c). When grafted with (*R*,*R*)-dach and (*S*,*S*)-dach, this material displayed a reversal in CO_2 adsorption step temperatures relative to the *R*-Mg_2(dobpdc) analogues (Figure 5c). This material, to which we refer as *S*-Mg_2(dobpdc), was thus identified as the enantiomer of *R*-Mg_2(dobpdc), and it exhibited ~92% enantiomeric purity and excellent sample quality on the basis of the CO_2 capacity of its dominant adsorption step. Qualitative characterization of the bare *R*- and *S*-Mg_2(dobpdc) materials using solid-state CD spectroscopy (measured via transmission and diffuse reflectance) confirmed that these materials are indeed enantiomers of each other (Figures 6a and S51–S53).

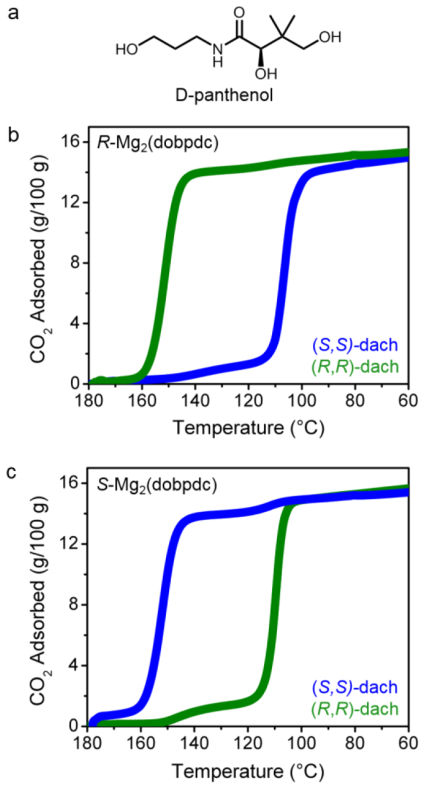

Figure 5. Characterization of enantiopure *R*- and *S*-Mg_2(dobpdc) obtained using D-panthenol as a chiral additive. (a) Structure of D-panthenol. (b) Pure CO_2 adsorption (cooling) isobars for (*R*,*R*)-dach (green) or (*S*,*S*)-dach (blue) appended to *R*-Mg_2(dobpdc). The relative step heights indicate 95% framework enantiopurity. (c) CO_2 adsorption (cooling) isobars for (*R*,*R*)-dach (green) or (*S*,*S*)-dach (blue) appended to *S*-Mg_2(dobpdc). The relative step heights indicate 92% purity.

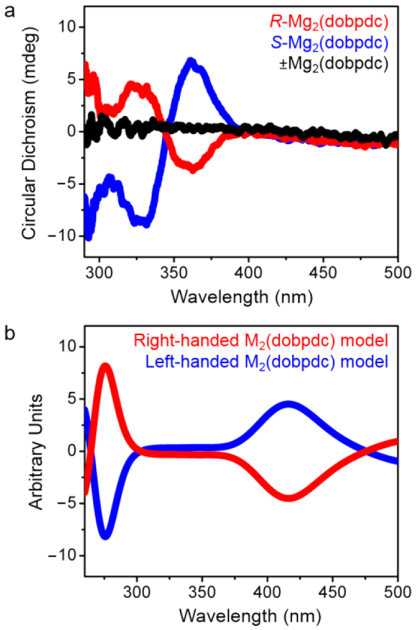

Figure 6. (a) Solid-state CD spectra of *R*- (red), *S*- (blue), and (±)-Mg_2(dobpdc) (black). The Mg_2(dobpdc) samples were mixed with KBr to form a tablet, and CD was detected in transmission geometry at 298 K. (b) Calculated CD spectra for right-handed (red) and left-handed (blue) Zn_2(dobpdc) based on a model segment of the structure containing three stacked dobpdc^{4-} molecules and six Zn^{2+} ions. See the Supporting Information for details.

To determine the absolute stereochemistries of *R*- and *S*-Mg_2(dobpdc), we compared their experimental solid-state CD spectra with calculated spectra for left- and right-handed M_2(dobpdc) enantiomers (i.e., materials exhibiting exclusively left- or right-handed helices, respectively) (Figure 6b). Computational models were prepared for several structural motifs of Zn_2(dobpdc), including one, two, or three stacked dobpdc^{4-} molecules coordinated to two, four, or six Zn^{2+} cations, respectively, as well as a segment of the metal–oxo helix consisting of seven truncated (one phenyl ring included) or seven full dobpdc^{4-} molecules (see Figure S54). The motifs corresponding to the left-handed (right-handed) structure all

DOI: 10.1021/jacs.7b09983
J. Am. Chem. Soc. 2017, 139, 16000–16012

exhibited an initial intense positive (negative) CD band in the UV−vis spectral region at wavelengths above 350 nm (peak positions were sensitive to the choice of the functional), except in the case of the truncated metal−oxo helix model, which exhibited weak intensity (Figure S56). Aggregation of multiple dobpdc^{4-} units led to an increase in the band intensities that was proportional to the number of dobpdc^{4-} units, while only minor qualitative changes were observed in the spectral shapes. The models therefore predict the presence of a CD band above ~350 nm that is caused predominantly by the twist direction of the dobpdc^{4-} moieties, followed by CD intensity of opposite sign at shorter wavelengths (Figure 6b). This sign pattern is in agreement with the experimental solid-state CD spectra (Figure 6a), and therefore, the calculations strongly support the assignment of *R*-Mg_2(dobpdc) and *S*-Mg_2(dobpdc) as being the right- and left-handed Mg_2(dobpdc) enantiomers (i.e., exhibiting right- and left-handed helices), respectively (Figures 6b and S54−S56).

The synthesis of Mg_2(dobpdc) in the presence of (±)-panthenol yielded (±)-Mg_2(dobpdc) (Figure S41), confirming that enantiopure panthenol is necessary for chiral induction. As expected, *R*-, *S*-, and (±)-Mg_2(dobpdc) produced identical powder X-ray diffraction patterns (Figure S47) and CO_2 adsorption isobars after grafting with (±)-dach (Figure S49). Scanning electron microscopy (SEM) further revealed very similar particle morphologies and sizes for these materials (Figure S48). Notably, after 7 months of storage in methanol, samples of both *S*-Mg_2(dobpdc) and *R*-Mg_2(dobpdc) exhibited no loss in enantiopurity or sample quality, as determined by characterization of CO_2 adsorption and relative step heights after grafting with enantiopure dach (Figure S50).

The synthesis of Mg_2(dobpdc) using the same D-panthenol solvent system and $Mg(NO_3)_2$:H_4dobpdc ratio with a range of H_4dobpdc concentrations indicated that a switch in Mg_2(dobpdc) handedness occurs between 107 and 140 mM H_4dobpdc (Figure 7). For H_4dobpdc concentrations greater than 140 mM, *S*-Mg_2(dobpdc) remained the predominant enantiomer. The mechanism leading to the switch in Mg_2(dobpdc) handedness is unclear, although we speculate that the mechanism for Mg_2(dobpdc) nucleation may be different depending on the reaction conditions and that D-panthenol may exert different stereochemical influences on the various nucleation species. However, because the mechanism of nucleation for Mg_2(dobpdc) is not known and it is in general extremely challenging to probe nucleation in metal−organic frameworks,[39] further investigation will be necessary to elucidate the mechanism of chiral induction by D-panthenol.

We attempted to obtain large, enantiopure single crystals of Zn_2(dobpdc) by growing them in the presence of D-panthenol (Table S4). However, using a D-panthenol:H_4dobpdc molar ratio of 3:1, 10:1, or 20:1 yielded only twinned single crystals exhibiting very slight chiral induction (Table S4), and higher molar quantities of D-panthenol (≥40) produced only polycrystalline powder. Notably, in the crystal structure of racemic Zn_2(dobpdc) synthesized with D-panthenol, DMA solvent molecules are bound to the metal sites in the framework, in spite of the presence of D-panthenol in the mother liquor. This structure is consistent with that of the crystals obtained as-synthesized without D-panthenol,[21] suggesting that D-panthenol does not bind strongly to the metal sites of the already-assembled Zn_2(dobpdc) framework and supporting the hypothesis that the role of D-panthenol in chiral induction may be related to M_2(dobpdc) nucleation rather than growth.

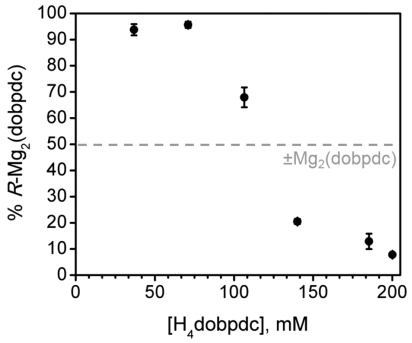

Figure 7. Plot illustrating the impact of varying H_4dobpdc concentration on the handedness of Mg_2(dobpdc) synthesized in the presence of D-panthenol. The same $Mg(NO_3)_2$:H_4dobpdc ratio was used for the different reactions.

The Structural Basis for Enantioselective Recognition of Ammonium Carbamate Chains. With a synthetic route in hand to access *R*- and *S*-Mg_2(dobpdc) frameworks with high enantiopurity, we could further investigate the structural basis for enantioselective recognition of chiral ammonium carbamate chains. Synchrotron powder X-ray diffraction patterns were obtained for (*R*,*R*)-dach−*R*-Mg_2(dobpdc) and (*S*,*S*)-dach−*R*-Mg_2(dobpdc) both before and after CO_2 capture (Figures S57−S62 and Tables S5 and S6). The powder patterns of CO_2-inserted (*R*,*R*)- and (*S*,*S*)-dach−*R*-Mg_2(dobpdc) were clearly distinct; upon CO_2 adsorption, (*R*,*R*)-dach−*R*-Mg_2(dobpdc) contracted more in the *ab* plane (0.15 Å) and expanded slightly more along the *c* axis (0.08 Å) compared with (*S*,*S*)-dach−*R*-Mg_2(dobpdc) (Table 1). Notably, the unit cell parameters of (±)-dach−Mg_2(dobpdc) were intermediate between those of (*R*,*R*)- and (*S*,*S*)-dach−Mg_2(dobpdc). As expected, the powder patterns of CO_2-inserted (*R*,*R*)-dach−*S*-Mg_2(dobpdc) and (*S*,*S*)-dach−*S*-Mg_2(dobpdc) were clearly distinct from each other (Figure S62). Rietveld refinements were performed in an attempt to determine the diastereomeric structures, but unfortunately it was not possible to precisely determine the positions of individual dach molecules (Figures S61 and S62).

Density functional theory (DFT) calculations provided further evidence for the absolute stereochemistries of *R*-Mg_2(dobpdc) and *S*-Mg_2(dobpdc). Models for CO_2-inserted (*R*,*R*)- and (*S*,*S*)-dach bound to *R*-Mg_2(dobpdc) (i.e., the enantiomer of Mg_2(dobpdc) containing right-handed helices) were prepared assuming the same unit cell and structure as (±)-dach−Zn_2(dobpdc). When the unit cell parameters were then allowed to vary freely during DFT structure optimization, the optimized (*R*,*R*)-dach−*R*-Mg_2(dobpdc) structure was contracted in the *ab* plane and expanded slightly along *c* relative to the (*S*,*S*)-dach structure (Table S8). These trends in the DFT results qualitatively match the experimental powder X-ray diffraction data and further confirm the stereochemical assignment obtained from solid-state CD spectra (Figure 6). Moreover, the calculated enthalpies for CO_2-inserted (*R*,*R*)- and (*S*,*S*)-dach−*R*-Mg_2(dobpdc) indicated that the (*R*,*R*) structure is more stable by approximately 80 kJ/mol (Figure S64), consistent with the more thermodynamically favorable CO_2 adsorption in (*R*,*R*)-dach−*R*-Mg_2(dobpdc) compared with (*S*,*S*)-dach−*R*-Mg_2(dobpdc) (Figure S7). Additional DFT calculations carried out assuming different unit cell parameters supported the conclusion that *R*-Mg_2(dobpdc) is the right-handed enantiomer of Mg_2(dobpdc) (Figure S64). Interestingly, CO_2-inserted

DOI: 10.1021/jacs.7b09983
J. Am. Chem. Soc. 2017, 139, 16000−16012

Table 1. Unit Cell Parameters Determined by Powder X-ray Diffraction for Dach-Appended Mg_2(dobpdc) Variants

	activated			CO_2-dosed		
	(*R*,*R*)-dach−*R*-Mg_2(dobpdc)	(±)-dach−(±)-Mg_2(dobpdc)	(*S*,*S*)-dach−*R*-Mg_2(dobpdc)	(*R*,*R*)-dach−*R*-Mg_2(dobpdc)	(±)-dach−(±)-Mg_2(dobpdc)	(*S*,*S*)-dach−*R*-Mg_2(dobpdc)
$a = b$/Å	21.1813(11)	21.4306(11)	21.3988(11)	20.4280(5)	20.5293(8)	20.5809(8)
c/Å	6.8612(5)	6.9107(5)	6.8697(5)	6.9667(3)	6.9401(4)	6.8861(4)
V/Å^3	2665.9(3)	2748.7(4)	2724.2(3)	2517.72(16)	2533.1(3)	2526.0(2)

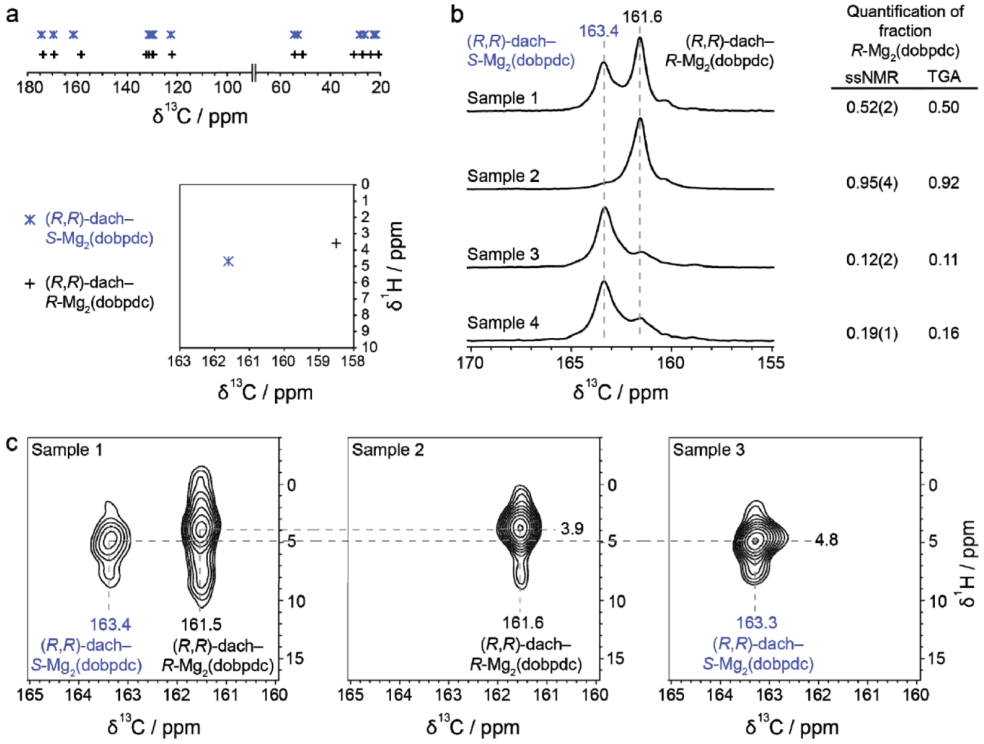

Figure 8. (a) (top) Calculated ^{13}C NMR chemical shifts from DFT structures for (*R*,*R*)-dach−*R*-Mg_2(dobpdc) and (*R*,*R*)-dach−*S*-Mg_2(dobpdc). The chemical shifts of greatest interest are those for the carbamate carbon, which occur at ~160 ppm and are different for the two structures. (bottom) DFT-calculated ^{1}H−^{13}C chemical shift correlations from DFT structure, assuming correlation only between the carbamate N−H (^{1}H) and the carbamate carbon (^{13}C). (b) Experimental magic-angle-spinning ^{13}C NMR (16.4 T) spectra for $^{13}CO_2$-inserted Mg_2(dobpdc) appended with (*R*,*R*)-dach. The gas-dosing pressures were 1050, 1047, 1027, and 1041 mbar for samples 1, 2, 3, and 4, respectively. Spectra were obtained by cross-polarization from ^{1}H with a contact time of 1 ms, and the sample spinning rate was 15 kHz. Two distinct resonances are visible at 163.4 and 161.6 ppm, which correspond to (*R*,*R*)-dach−*S*-Mg_2(dobpdc) and (*R*,*R*)-dach−*R*-Mg_2(dobpdc), respectively. The intensities of the two resonances varied for different batches of Mg_2(dobpdc). Quantification of the *R*-Mg_2(dobpdc):*S*-Mg_2(dobpdc) ratio by solid-state NMR spectroscopy agreed well with TGA quantification on the same samples (right). (c) Experimental 2D HETCOR magic-angle-spinning NMR (16.4 T) spectra for samples 1, 2, and 3 shown in (b). The sample spinning rate was 15 kHz. A short contact time of 100 μs was used in this experiment, such that the major correlation is between the carbamate N−H hydrogens and the carbamate carbon. Distinct chemical shifts are observed for the carbamate N−H hydrogens of (*R*,*R*)-dach−*S*-Mg_2(dobpdc) and (*R*,*R*)-dach−*R*-Mg_2(dobpdc), in good agreement with the DFT calculations shown in (a). NMR experiments were carried out under ambient conditions without sample temperature control.

(*R*,*R*)-dach−*R*-Mg_2(dobpdc) was found to be more stable than CO_2-inserted (*S*,*S*)-dach−*R*-Mg_2(dobpdc) in all of the DFT calculations, regardless of what unit cell parameters were assumed, indicating that greater stability in the DFT calculations was not caused simply by contraction in the *ab* plane.

We employed solid-state NMR spectroscopy to further characterize the diastereomeric ammonium carbamate phases and to confirm the absolute stereochemistries of *R*- and *S*-Mg_2(dobpdc). DFT calculations for (*R*,*R*)- and (*S*,*S*)-dach−*R*-Mg_2(dobpdc) showed distinct chemical shifts for the carbamate carbon, carbamate N−H hydrogen, and ammonium hydrogen atoms (Figures 8a, S65, and S66 and Table S7), as anticipated for diastereomeric structures.[40] The ability of DFT to accurately optimize candidate structures of crystalline materials and predict NMR parameters is now well-established, and comparison of experimental and calculated parameters (in particular ^{1}H chemical shifts) for different trial structures can facilitate structure determination.[41−46] Experimental magic-angle-spinning solid-state NMR spectra were collected for dach−Mg_2(dobpdc) variants following dosing with isotopically enriched (99% ^{13}C) CO_2.[24] Cross-polarization from ^{1}H to ^{13}C enabled selective detection of chemisorbed CO_2 and eliminated background signal from gas-phase CO_2. Carbon resonances from the dobpdc^{4-} linker and the diamine alkyl backbone are visible in these spectra, although the intensities are much weaker because ^{13}C is present in natural abundance (1%) at these positions.

Carbon dioxide chemisorbed in the (*R*,*R*)-dach−*R*-Mg_2(dobpdc) and (*R*,*R*)-dach−*S*-Mg_2(dobpdc) frameworks

DOI: 10.1021/jacs.7b09983
J. Am. Chem. Soc. 2017, 139, 16000−16012

exhibits distinct ^{13}C chemical shifts, consistent with the DFT calculations (Figure 8b). The spectrum of the (*R*,*R*)-dach−*S*-Mg_2(dobpdc) framework displays a major chemisorbed CO_2 resonance at 163.4 ppm, a value that is similar to resonances observed for other ammonium carbamate chains formed in this material.[24] In contrast, the (*R*,*R*)-dach−*R*-Mg_2(dobpdc) framework exhibits a major CO_2 resonance at 161.6 ppm, which is closer to chemical shifts previously observed for carbamic acids in metal−organic frameworks[24,47] and may be indicative of stronger carbamate ion-pairing in this diastereomeric phase.

Importantly, the qualitative agreement between the theoretical and measured ^{13}C chemical shifts for chemisorbed CO_2 further supports our earlier assignment of *R*-Mg_2(dobpdc) and *S*-Mg_2(dobpdc) as the right- and left-handed structures, respectively. In contrast to the enantiopure dach−Mg_2(dobpdc) structures, ^{13}C solid-state NMR spectroscopic characterization of (±)-dach−(±)-Mg_2(dobpdc) revealed a single broad feature at ∼162 ppm, suggestive of a distribution of different local chemical environments for the carbamate that arises due to the random statistical distribution of (*R*,*R*)- and (*S*,*S*)-dach within the crystallites (Figure S68).

The ^{13}C NMR spectra also enabled quantitation of the Mg_2(dobpdc) enantiopurity, corroborating the values determined from the TGA step height assay (Figure 8b). Quantitation of CO_2-inserted (*R*,*R*)-dach−(±)-Mg_2(dobpdc) by solid-state NMR spectroscopy indicates a 1:1 ratio (within error) of *R*- and *S*-Mg_2(dobpdc), confirming the validity of the NMR quantitation approach (see the Experimental Section for further details). Similarly, the enantiopurities extracted from these NMR experiments agree well with the values determined using TGA step height quantification for 95%, 19%, and 12% *R*-Mg_2(dobpdc) (Figure 8b).

Further insight into the diastereomeric structures was gained using two-dimensional heteronuclear correlation (HETCOR) solid-state NMR spectroscopy. In this experiment, cross-polarization from ^{1}H to ^{13}C enables detection of chemisorbed $^{13}CO_2$ while also revealing the ^{1}H chemical shifts of the hydrogen atoms most proximal to the carbamate carbon. For both (*R*,*R*)-dach−*R*-Mg_2(dobpdc) and (*R*,*R*)-dach−*S*-Mg_2(dobpdc) phases, the strongest correlations with the ^{13}C carbamate carbon arise from the carbamate N−H hydrogen, an unsurprising result because this hydrogen is the closest through space. The chemical shifts of the N−H hydrogen atoms are 3.9 and 4.8 ppm, respectively, for (*R*,*R*)-dach−*R*-Mg_2(dobpdc) and (*R*,*R*)-dach−*S*-Mg_2(dobpdc) (Figure 8c), consistent with the DFT-calculated chemical shifts within 0.3 ppm and further supporting our assignments of *R*- and *S*-Mg_2(dobpdc) (Figure 8a).

In HETCOR experiments carried out with longer contact times, correlations between the ^{13}C carbamate carbon and the ammonium hydrogen atoms were also detected (Figure S69), and the ^{1}H chemical shifts for the ammonium hydrogen atoms were found to be 7.8 and 7.2 ppm for (*R*,*R*)-dach−*R*-Mg_2(dobpdc) and (*R*,*R*)-dach−*S*-Mg_2(dobpdc), respectively. Differences in chemical shifts of specific nuclei between the two diastereomers can be correlated to differences in the strengths of non-covalent interactions, with larger ^{1}H chemical shifts indicative of stronger hydrogen bonding.[48] Our results thus indicate the presence of stronger hydrogen bonding for the ammonium hydrogen atoms of (*R*,*R*)-dach−*R*-Mg_2(dobpdc) and weaker hydrogen bonding for the carbamate N−H hydrogens relative to (*S*,*S*)-dach−*R*-Mg_2(dobpdc).

Taking into account all of the data, a detailed explanation can be proposed for the different thermodynamic stabilities of the diastereomeric phases. Figure 9 presents DFT-calculated structures for (*R*,*R*)-dach−*R*-Mg_2(dobpdc) and (*S*,*S*)-dach−*R*-Mg_2(dobpdc), with unit cell parameters fixed to the values determined by powder X-ray diffraction (with the (*R*,*R*)-dach structure slightly more contracted in the *ab* plane and slightly expanded along the *c* axis). Space-filling models reveal more extensive van der Waals contacts for the (*R*,*R*)-dach ammonium carbamates compared with the (*S*,*S*)-dach ones, both with respect to interactions between cyclohexane rings and between the rings and the pore walls (Figure 9a). It is likely that more favorable van der Waals contacts and thus superior packing of (*R*,*R*)-dach stabilizes the resulting ammonium carbamate structure.

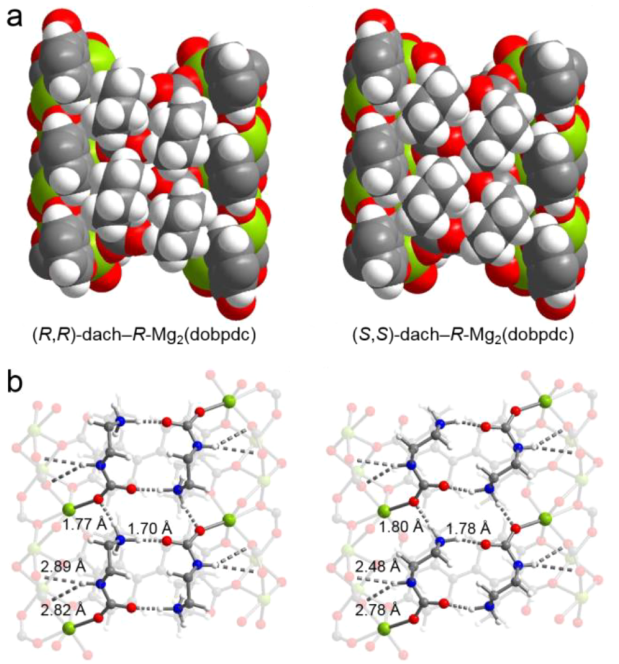

Figure 9. DFT-calculated structures of the CO_2-inserted diastereomeric phases of dach−Mg_2(dobpdc). Light-green, blue, red, gray, and white spheres represent Mg, N, O, C, and H atoms, respectively. (a) Space-filling models of the CO_2-inserted structures of (*R*,*R*)-dach−*R*-Mg_2(dobpdc) (left) and (*S*,*S*)-dach−*R*-Mg_2(dobpdc) (right) reveal more extensive van der Waals contacts between the cyclohexane groups and the dobpdc^{4-} pore walls for the (*R*,*R*)-dach structure. (b) The (*R*,*R*)- and (*S*,*S*)-dach structures also display subtly different hydrogen-bonding networks. The (*R*,*R*)-dach−*R*-Mg_2(dobpdc) structure (left) exhibits stronger ammonium hydrogen bonds, both in the *ab* plane and along *c*, and weaker carbamate N−H hydrogen bonds with the framework walls relative to (*S*,*S*)-dach−*R*-Mg_2(dobpdc) (right).

The stronger ammonium hydrogen bonding in CO_2-inserted (*R*,*R*)-dach−*R*-Mg_2(dobpdc) compared with the (*S*,*S*)-dach structure is also evident from the shorter H···O distances in the *ab* plane and along the *c* axis and the N−H···O angle that more closely approaches 180° in the *ab* plane (see Figures 9b and S67 and Tables S9−S12).[48] The shorter and therefore stronger carbamate N−H hydrogen bonding in the (*S*,*S*)-dach structure can be explained by a bifurcated hydrogen bond (i.e., approximately equal angles) with two carboxylate oxygens from the framework with lengths of 2.48 and 2.78 Å. In contrast, the carbamate N−H of (*R*,*R*)-dach is oriented toward a single carboxylate oxygen with a relatively long hydrogen-bond length of 2.82 Å. The greater overall stability of the (*R*,*R*)-dach−*R*-

DOI: 10.1021/jacs.7b09983
J. Am. Chem. Soc. 2017, 139, 16000−16012

Mg_2(dobpdc) structure, based on isobaric CO_2 adsorption and DFT calculations, suggests that stronger ammonium hydrogen bonding compensates for its weaker N−H carbamate hydrogen bonding.

We propose a few roles that the chiral *R*-Mg_2(dobpdc) framework may play in the observed distinct hydrogen-bonding strengths between the diastereomeric phases. The stronger hydrogen bonding in the (*R*,*R*)-dach structure could arise from superior packing of the cyclohexane rings, enabling more optimal orientation of the ammonium hydrogens and carbamate oxygen for hydrogen bonding (Figure 9b). In addition, the stereochemistry of the two-carbon diamine bridge in (*R*,*R*)-dach leads to a different orientation of the ammonium C−N bond, thereby subtly affecting the positions of the ammonium hydrogen atoms and the carbamate oxygen (Figure 9b). The framework influences the ammonium carbamate stability not only by direct interactions (through hydrophobic packing and hydrogen bonding with the carbamate N−H group) but also by serving as a chiral three-dimensional scaffold that impacts the strength of interactions between the enantiopure ammonium carbamates.

Because the enantioselective interactions in dach−M_2(dobpdc) appear to be strongly correlated with contraction of the framework structure due to hydrogen bonding, it was unclear whether M_2(dobpdc) would exhibit broad enantioselectivity toward guest molecules that do not induce a unit cell contraction in the *ab* plane. Therefore, Mg_2(dobpdc) was evaluated for enantioselectivity in the formation of ammonium carbamate chains from another chiral diamine, 3-aminopyrrolidine (Figures S70−S74). The diamine *S*-3-aminopyrrolidine results in two adsorption steps upon grafting to (±)-Mg_2(dobpdc), while the racemic diamine counterpart exhibits a single step, indicating enantioselective recognition by Mg_2(dobpdc) (Figure S73). Therefore, the enantioselective recognition of diverse diamine structures by Mg_2(dobpdc) is promising in terms of its generality for recognizing different chiral guest molecules.

CONCLUSION

The foregoing results demonstrate enantioselective recognition of chiral ammonium carbamate chains by M_2(dobpdc), as revealed by CO_2 adsorption experiments. To better understand the structural basis of enantioselective recognition, a procedure to isolate enantiopure Mg_2(dobpdc) was devised. Surprisingly, a single chiral additive, D-panthenol, could be used to prepare either *R*- or *S*-Mg_2(dobpdc) with high enantiopurity, depending on the reactant concentrations. The high enantiopurities and crystallinities of both *R*- and *S*-Mg_2(dobpdc) enabled further investigation into the chiral ammonium carbamate structures. This study revealed that subtle enantioselective interactions between the ammonium carbamates and the chiral M_2(dobpdc) framework have a substantial impact on the affinity of chiral-diamine-appended M_2(dobpdc) for CO_2. In addition, the chiral Mg_2(dobpdc) scaffolding influences the relative orientations of the ammonium carbamate chains and the strength of their hydrogen-bonding interactions both in the *ab* plane and along the *c* axis.

In conjunction with the other valuable characteristics of M_2(dobpdc), including low cost, scalable synthesis, excellent stability, large pore diameter (18 Å), and postsynthetic tunability, the discovery of a synthetic route for enantiopure Mg_2(dobpdc) opens up an array of potential applications for this promising and versatile framework. While further work is required to establish chiral recognition of guest molecules (or transition states) in solution, the detailed structural study performed here highlights the importance of one-dimensional channels and guest−guest interactions for enantioselectivity in this material. Future efforts will be directed toward exploring the enantioselective adsorption of guests capable of binding simultaneously to multiple open metal coordination sites and exploiting stabilizing interactions between bound guest molecules.

EXPERIMENTAL SECTION

General Procedures, Materials, and Reagents. ^{1}H NMR spectra were collected on a Bruker AV-300 MHz NMR spectrometer, a Bruker AVB-400 MHz NMR spectrometer, or a Bruker AVQ-400 MHz NMR spectrometer, as indicated in the figure captions in the Supporting Information. Laboratory powder X-ray diffraction patterns were collected using a Bruker AXS D8 Advance diffractometer with Cu Kα radiation (λ = 1.5418 Å). All synthetic manipulations were carried out under air unless noted otherwise. All solvents and diamines were purchased from commercial sources and used without additional purification. All chiral additives were purchased from commercial vendors and used without purification. The ligand H_4dobpdc was purchased from Hangzhou Trylead Chemical Technology Co.

Multigram Synthesis of Racemic Mg_2(dobpdc). Racemic Mg_2(dobpdc) was synthesized on a multigram scale following a published procedure with slight modifications. The ligand H_4dobpdc (9.89 g, 36.1 mmol) and $Mg(NO_3)_2{\cdot}6H_2O$ (11.5 g, 44.9 mmol) were dissolved in 200 mL of 55:45 methanol/DMF using sonication. The solution was filtered to remove any undissolved particulates and added to a 350 mL glass pressure vessel with a 3 cm Teflon-coated stir bar. The reactor was sealed with a Teflon cap and heated in a silicone oil bath at 120 °C for 20 h with vigorous stirring (stirring rate of at least 750 rpm). The white powder was isolated by filtration and soaked three times in 200 mL of DMF for a minimum of 3 h at 60 °C followed by solvent exchange by soaking three times in 200 mL of methanol for a minimum of 3 h at 60 °C.

Synthesis of Optimized *R*-Mg_2(dobpdc) and *S*-Mg_2(dobpdc) Using D-Panthenol as a Chiral Additive. For the synthesis of *R*-Mg_2(dobpdc), a 20 mL scintillation vial was charged with the ligand H_4dobpdc (101 mg, 0.370 mmol, 1.00 equiv) and $Mg(NO_3)_2{\cdot}6H_2O$ (127 mg, 0.500 mmol, 1.34 equiv). Separately, DMF (3.03 mL) and D-panthenol (2.94 g, 14.3 mmol, 39:1 D-panthenol:H_4dobpdc molar ratio) were mixed in a glass jar, and the mixture was heated with a heat gun and gently agitated until all of the D-panthenol had dissolved. Methanol (4.25 mL) was added to the DMF/D-panthenol mixture, and the resulting mixture was gently agitated to make the solution homogeneous. Finally, the DMF/methanol/D-panthenol solvent system was added, along with a Teflon-coated magnetic stirring bar, to the 20 mL vial containing H_4dobpdc and $Mg(NO_3)_2{\cdot}6H_2O$. Sonication was not used to dissolve the solids. The threads of the glass vial were wrapped in Teflon tape, and the vial was tightly sealed with a Teflon-lined cap. The solution was then heated at 120 °C in a heating block for 20 h with vigorous stirring (stirring rate of at least 750 rpm), during which time a white solid precipitated from the solution. The vial was cooled to room temperature and filtered, and the resulting solid was washed thoroughly with fresh DMF (15 mL). The solid was transferred to a vial filled with fresh DMF (10 mL) and allowed to soak at 120 °C for 24 h. The supernatant was decanted and replaced with fresh DMF (10 mL). This process was repeated a total of three times. The DMF was replaced with methanol (10 mL), and the off-white solid was soaked in methanol at 60 °C for 3 h. The supernatant was decanted and replaced with fresh methanol (10 mL). This process was repeated a total of three times. For the synthesis of optimized *S*-Mg_2(dobpdc) using D-panthenol as a chiral additive, the procedure was identical to that described above for *R*-Mg_2(dobpdc) except that 508 mg of H_4dobpdc (1.85 mmol, 1.00 equiv) and 622 mg of $Mg(NO_3)_2{\cdot}6H_2O$ (2.43 mmol, 1.32 equiv) were used. Experimental details are provided in the Supporting Information for the gram-scale syntheses of *R*-Mg_2(dobpdc) and *S*-Mg_2(dobpdc) using D-panthenol and for the small-scale synthesis of Mg_2(dobpdc) in the presence of various chiral additives.

DOI: 10.1021/jacs.7b09983
J. Am. Chem. Soc. 2017, 139, 16000−16012

Synthesis of Mg_2(pc-dobpdc). Mg_2(pc-dobpdc) was synthesized, washed, and characterized following a previously published procedure.[23]

Synthesis of Diamine-Appended Variants of Mg_2(dobpdc) and Mg_2(pc-dobpdc). A 20 mL scintillation vial was charged with toluene (4 mL) and the diamine (1 mL). In the case of enantiopure dach, the diamine (0.5 g) was dissolved in chloroform with 0.75% ethanol (5 mL), and extensive sonication was used to dissolve as much of the solid diamine as possible. The methanol-solvated metal−organic framework (~20 mg) was filtered and washed with toluene (20 mL) or with chloroform with 0.75% ethanol (1−5 mL) in the case of enantiopure dach samples. (Note: the framework should not be allowed to dry completely, as doing so for an extended period can decrease crystallinity and surface area.) It should be noted that for some Mg_2(dobpdc) batches, washing with >5 mL of chloroform with 0.75% ethanol caused diamine loss. The framework was added to the diamine solution, and the vial was swirled several times and allowed to stand at room temperature for 12−48 h (the grafting time was not found to substantially affect the amount of amine grafted). At this time, the mixture was filtered, and the resulting powder was thoroughly washed with toluene or chloroform with 0.75% ethanol (20 mL) and allowed to dry for several minutes, yielding ~30 mg of the diamine-appended metal−organic framework. Diamine loadings were determined by suspending ~5 mg of the diamine-appended metal−organic framework in 0.5 mL of DMSO-d_6, adding several drops of DCl (35 wt % in D_2O), heating until the mixture became homogeneous, and analyzing the resulting solution by ^{1}H NMR spectroscopy.

Synthesis of Zn_2(dobpdc) Single Crystals. Racemic twinned single crystals of Zn_2(dobpdc) were synthesized as described previously.[21] Attempts to synthesize enantiopure Zn_2(dobpdc) single crystals by adding D-panthenol are detailed in the Supporting Information.

Synthesis of Diamine-Appended Zn_2(dobpdc) Single Crystals. Samples of Zn_2(dobpdc) crystals were removed from storage in a N_2 glovebox under 2 mL of toluene in individual 4 mL vials. Subsequently, (±)-dach (12 μL) was added to the vial in air, and the vial was then left undisturbed for 4 h. Excess diamine was removed by decanting and washing three times with fresh toluene in air at 60 °C (first wash, 1 h; subsequent washes, 10 min each). The supernatant was then exchanged three times with dry hexanes in air (room temperature, 5 min per wash) to facilitate removal of residual solvent from the framework pores. Crystals were analyzed by single-crystal X-ray diffraction within 24 h of preparation. Details for grafting of (±)-dach and (*R*,*R*)-dach to Zn_2(dobpdc) powder samples are provided in the Supporting Information. Experimental details for single-crystal X-ray diffraction are provided in the Supporting Information.

Thermogravimetric Analysis. TGA experiments were conducted at ambient total pressure using a TA Instruments TGA Q5000 instrument, except for the 0.1 °C/min isobars shown in Figures S5 and S6, which were measured using a TA Instruments Discovery Classic TGA instrument, which has an equivalent furnace and gas flow design. For CO_2 adsorption/desorption experiments, samples were activated under flowing N_2 for 20−30 min until the mass stabilized; exact activation conditions for each diamine-appended material were determined by careful analysis of the dry N_2 thermal decomposition profiles. After activation, the gas stream was switched to pure CO_2, and samples were cooled using a ramp rate of 2 °C/min unless specified otherwise in the figure legends. Masses were uncorrected for buoyancy effects. Dry N_2 decomposition experiments were carried out using a heating ramp rate of 1.5 °C/min unless specified otherwise in the figure legends.

Synchrotron Powder X-ray Diffraction of dach−Mg_2(dobpdc) Variants. Activated samples were prepared by heating freshly prepared dach−Mg_2(dobpdc) variants (25 mg) under flowing argon at 155 °C for 2 h. The samples were allowed to cool to room temperature, transferred to a N_2-filled glovebag, and then gently ground into fine powders using a mortar and pestle. The ground powders were tightly packed into 1.0 mm borosilicate glass capillaries, and the outlets were plugged with vacuum grease, after which the capillaries were removed from the glovebag and flame-sealed. CO_2-dosed samples were prepared by placing freshly prepared dach−Mg_2(dobpdc) variants (10 mg) onto a thermogravimetric analyzer, activating them under flowing N_2 for 30 min at 180 °C, and then cooling them to 30 °C before switching the gas stream to pure CO_2. After 20 min, CO_2-dosed samples were removed from the furnace of the thermogravimetric analyzer, gently ground into fine powders under air, and packed into 1.0 mm diameter borosilicate glass capillaries and flame-sealed. It should be noted that CO_2 does not desorb from these materials under air at room temperature (Figures S12−S14).

High-resolution powder X-ray diffraction patterns of flame-sealed samples as well as in situ CO_2-dosed samples were collected with synchrotron X-ray radiation at beamline 17-BM-B at the Advanced Photon Source at Argonne National Laboratory. The wavelength of the X-rays was 0.45241 Å, and the diffracted X-rays were recorded by a PerkinElmer α-Si flat panel detector. An Oxford Cryosystems cryostream was used to control the experimental temperature of the samples during data collection.

Prior to in situ dosing of CO_2 and measurement of powder X-ray diffraction patterns, ~5 mg of sample was packed into borosilicate glass capillaries of 1 mm diameter in air. Each capillary was attached to a custom-designed gas-dosing cell equipped with a gas valve and was then transferred to the goniometer head. All of the adsorbed air was removed by evacuation in situ using a turbomolecular pump. After activation at 150 °C, variable pressures of CO_2 were dosed to the samples, and the cryostream was used to change the temperature between 500 and 100 K. Analysis of all diffraction data (including Pawley and Rietveld refinement of the data) is detailed in the Supporting Information.

Solid-State Circular Dichroism Spectroscopy Experiments. All of the solid-state CD measurements were performed on a J-1500 CD spectrometer (JASCO) and measured via transmission or diffuse reflectance. Additional experimental details are provided in the Supporting Information.

Solid-State Magic-Angle-Spinning ^{13}C NMR Experiments. A freshly prepared dach-appended Mg_2(dobpdc) variant (50−100 mg) was activated under flowing argon at 155 °C for 2 h. The sample was allowed to cool to room temperature and then transferred to a N_2-filled glovebag. The samples were then packed into 3.2 mm zirconia rotors. Uncapped rotors were then evacuated for at least 10 min inside a home-built gas-dosing manifold before dosing with isotopically enriched $^{13}CO_2$ (99 atom % ^{13}C, <3 atom % ^{18}O, Sigma-Aldrich), after which the samples were allowed to equilibrate for at least 1 h. The home-built gas-dosing manifold was recently described elsewhere.[24] This manifold allows rotors to be sealed under controlled gas pressures. Gas dosing was carried out at ambient temperature (~22 °C). Additional experimental details and description of peak quantification are provided in the Supporting Information.

Density Functional Theory Calculations. DFT calculations for CO_2-inserted dach-appended M_2(dobpdc) were performed using the CASTEP code.[49] The PBE (with a generalized gradient approximation) functional was used for the exchange−correlation term,[50] and ultrasoft pseudopotentials were used.[51] Calculations used plane-wave basis functions with an energy cutoff of 60 Ry and a *k*-point spacing of 0.06 Å^{-1}, parameters that were recently found to give converged ^{1}H and ^{13}C chemical shifts to within 0.1 ppm for materials closely related to those studied here.[24] NMR calculations were performed using the gauge including projector augmented wave (GIPAW) approach.[52] Calculated chemical shifts, δ_{iso}, were obtained using $\delta_{iso} = -(\sigma_{iso} - \sigma_{ref})$, where σ_{iso} is the calculated isotropic shielding and σ_{ref} is a reference value. For ^{1}H NMR, a σ_{ref} value of 30.5 ppm was used,[53,54] and for ^{13}C NMR, a σ_{ref} value of 170.6 ppm was used.[24] Initial diastereomeric structural models were generated from the single-crystal structure of CO_2-inserted (±)-dach−Zn_2(dobpdc). For the NMR calculations presented in the text, we fixed the unit cell parameters to the values obtained from powder X-ray diffraction given our assignments of *R*- and *S*-Mg_2(dobpdc). Prior to the NMR calculation, a geometry optimization was carried out in which the unit cell parameters were fixed but the atomic positions were allowed to vary. Additional NMR calculations with different assignments of the unit cell parameters showed only small variations of chemical shift (on the order of 0.2 ppm). Additional details of the unit cell parameters and geometry optimizations are given in the Supporting Information. Details regarding the time-dependent DFT

DOI: 10.1021/jacs.7b09983
J. Am. Chem. Soc. 2017, 139, 16000−16012

calculations to simulate CD spectra[55,56] are provided in the Supporting Information.

Scanning Electron Microscopy. SEM samples of Mg_2(dobpdc) were prepared by dispersing fine powders into methanol and drop-casting the mixture onto a silicon chip. To dissipate charge, the samples were sputter-coated with approximately 3 nm of Au (Denton Vacuum). Crystals were imaged at 5 keV and 12 μA using a field-emission scanning electron microscope (JEOL FSM6430).

■ ASSOCIATED CONTENT

Supporting Information

The Supporting Information is available free of charge on the ACS Publications website at DOI: 10.1021/jacs.7b09983.

Crystallographic data for Zn_2(dobpdc)(±dach−CO_2)$_2$ (CIF)

Additional experimental details, additional gas adsorption data, TGA decomposition traces, digestion experiments and ^{1}H NMR spectroscopy, powder X-ray diffraction, calculations of differential enthalpy and entropy of adsorption, Rietveld and Pawley refinements, screening of chiral additives, scanning electron microscopy, additional experimental and calculated solid-state CD spectra, calculated enthalpies from DFT, calculated hydrogen-bond distances and angles from DFT, and additional solid-state NMR spectra (PDF)

■ AUTHOR INFORMATION

Corresponding Author

*jrlong@berkeley.edu

ORCID

Alexander C. Forse: 0000-0001-9592-9821

Monika Srebro-Hooper: 0000-0003-4211-325X

Jochen Autschbach: 0000-0001-9392-877X

Jeffrey R. Long: 0000-0002-5324-1321

Notes

The authors declare the following competing financial interest(s): U.C. Berkeley has applied for a patent on some of the materials discussed herein, on which J.D.M., L.B.P.-Z., and J.R.L. are included as inventors. J.R.L. has a financial interest in Mosaic Materials, Inc., a startup company working to commercialize metal−organic frameworks for gas separations.

■ ACKNOWLEDGMENTS

This research was supported by the Center for Gas Separations Relevant to Clean Energy Technologies, an Energy Frontier Research Center supported by the U.S. Department of Energy, Office of Science, Office of Basic Energy Sciences, under Award DE-SC0001015. Preliminary characterization of CO_2 adsorption in dach−Mg_2(dobpdc) was funded by the Advanced Research Projects Agency—Energy (ARPA-E), U.S. Department of Energy, under Award DE-AR0000402. Single-crystal X-ray diffraction data were collected on beamline 11.3.1 at the Advanced Light Source at Lawrence Berkeley National Laboratory, which is supported by the Director, Office of Science, Office of Basic Energy Sciences, U.S. Department of Energy, under Contract DE-AC02-05CH11231. Synchrotron powder X-ray diffraction data used the resources of the Advanced Photon Source, a DOE Office of Science User Facility operated for the DOE Office of Science by Argonne National Laboratory under Contract DE-AC02-06CH11357. The DFT calculations were performed at the Molecular Graphics and Computation Facility (College of Chemistry, UC Berkeley), which is supported by NIH Grant S10OD023532. We thank the Miller Institute for Basic Research in Science for postdoctoral fellowship support of J.D.M., SURF Rose Hills for support of L.B.P.-Z. through a summer research fellowship, the Philomathia Foundation and Berkeley Energy and Climate Institute for support of A.C.F., the National Science Foundation for support of J.O. through a graduate research fellowship, the National Institutes of Health for support of P.J.M. through a postdoctoral fellowship (GM120799), the National Science Foundation for support of J.A. through Grant CHE-1560881, and the Center for Computational Research (CCR) at the University at Buffalo for providing computational resources to J.A. and M.S.-H. We further thank Leah Pandiscia and Wayne Kottkamp of JASCO for facilitating the solid-state CD experiments, Henry Jiang for experimental assistance with synchrotron powder X-ray diffraction, and Dr. Katie R. Meihaus for editorial assistance.

■ REFERENCES

(1) Lin, G.-Q.; You, Q.-D.; Cheng, J.-F. *Chiral Drugs: Chemistry and Biological Action*; John Wiley & Sons: Hoboken, NJ, 2011.

(2) Nguyen, L. A.; He, H.; Pham-Huy, C. *Int. J. Biomed. Sci.* **2006**, *2* (2), 85.

(3) Navarro-Sánchez, J.; Argente-García, A. I.; Moliner-Martínez, Y.; Roca-Sanjuán, D.; Antypov, D.; Campíns-Falcó, P.; Rosseinsky, M. J.; Martí-Gastaldo, C. *J. Am. Chem. Soc.* **2017**, *139* (12), 4294.

(4) Li, G.; Yu, W.; Cui, Y. *J. Am. Chem. Soc.* **2008**, *130* (14), 4582.

(5) Padmanaban, M.; Muller, P.; Lieder, C.; Gedrich, K.; Grunker, R.; Bon, V.; Senkovska, I.; Baumgartner, S.; Opelt, S.; Paasch, S.; Brunner, E.; Glorius, F.; Klemm, E.; Kaskel, S. *Chem. Commun.* **2011**, *47* (44), 12089.

(6) Kuang, X.; Ma, Y.; Su, H.; Zhang, J.; Dong, Y.-B.; Tang, B. *Anal. Chem.* **2014**, *86* (2), 1277.

(7) Peng, Y.; Gong, T.; Zhang, K.; Lin, X.; Liu, Y.; Jiang, J.; Cui, Y. *Nat. Commun.* **2014**, *5*, 4406.

(8) Seo, J. S.; Whang, D.; Lee, H.; Jun, S. I.; Oh, J.; Jeon, Y. J.; Kim, K. *Nature* **2000**, *404* (6781), 982.

(9) Dang, D.; Wu, P.; He, C.; Xie, Z.; Duan, C. *J. Am. Chem. Soc.* **2010**, *132* (41), 14321.

(10) Ma, L.; Falkowski, J. M.; Abney, C.; Lin, W. *Nat. Chem.* **2010**, *2* (10), 838.

(11) Yoon, M.; Srirambalaji, R.; Kim, K. *Chem. Rev.* **2012**, *112* (2), 1196.

(12) Banerjee, M.; Das, S.; Yoon, M.; Choi, H. J.; Hyun, M. H.; Park, S. M.; Seo, G.; Kim, K. *J. Am. Chem. Soc.* **2009**, *131* (22), 7524.

(13) Cho, S.-H.; Ma, B.; Nguyen, S. T.; Hupp, J. T.; Albrecht-Schmitt, T. E. *Chem. Commun.* **2006**, No. 24, 2563.

(14) Morris, R. E.; Bu, X. *Nat. Chem.* **2010**, *2* (5), 353.

(15) Zhang, J.; Chen, S.; Wu, T.; Feng, P.; Bu, X. *J. Am. Chem. Soc.* **2008**, *130* (39), 12882.

(16) Bisht, K. K.; Suresh, E. *J. Am. Chem. Soc.* **2013**, *135* (42), 15690.

(17) Lin, Z.; Slawin, A. M. Z.; Morris, R. E. *J. Am. Chem. Soc.* **2007**, *129* (16), 4880.

(18) Hao, X.-R.; Wang, X.-L.; Qin, C.; Su, Z.-M.; Wang, E.-B.; Lan, Y.-Q.; Shao, K.-Z. *Chem. Commun.* **2007**, No. 44, 4620.

(19) McDonald, T. M.; Lee, W. R.; Mason, J. A.; Wiers, B. M.; Hong, C. S.; Long, J. R. *J. Am. Chem. Soc.* **2012**, *134* (16), 7056.

(20) McDonald, T. M.; Mason, J. A.; Kong, X.; Bloch, E. D.; Gygi, D.; Dani, A.; Crocella, V.; Giordanino, F.; Odoh, S. O.; Drisdell, W. S.; Vlaisavljevich, B.; Dzubak, A. L.; Poloni, R.; Schnell, S. K.; Planas, N.; Lee, K.; Pascal, T.; Wan, L. F.; Prendergast, D.; Neaton, J. B.; Smit, B.; Kortright, J. B.; Gagliardi, L.; Bordiga, S.; Reimer, J. A.; Long, J. R. *Nature* **2015**, *519* (7543), 303.

(21) Siegelman, R. L.; McDonald, T. M.; Gonzalez, M. I.; Martell, J. D.; Milner, P. J.; Mason, J. A.; Berger, A. H.; Bhown, A. S.; Long, J. R. *J. Am. Chem. Soc.* **2017**, *139* (30), 10526.

(22) Rosi, N. L.; Kim, J.; Eddaoudi, M.; Chen, B.; O'Keeffe, M.; Yaghi, O. M. *J. Am. Chem. Soc.* **2005**, *127* (5), 1504.

DOI: 10.1021/jacs.7b09983
J. Am. Chem. Soc. 2017, 139, 16000−16012

(23) Milner, P. J.; Martell, J. D.; Siegelman, R. L.; Gygi, D.; Weston, S. C.; Long, J. R. 2017, in review.
(24) Milner, P. J.; Siegelman, R. L.; Forse, A. C.; Gonzalez, M. I.; Runčevski, T.; Martell, J. D.; Reimer, J. A.; Long, J. R. *J. Am. Chem. Soc.* **2017**, *139* (38), 13541.
(25) Mosaic Materials, Inc. http://mosaicmaterials.com/.
(26) Jo, H.; Lee, W. R.; Kim, N. W.; Jung, H.; Lim, K. S.; Kim, J. E.; Kang, D. W.; Lee, H.; Hiremath, V.; Seo, J. G.; Jin, H.; Moon, D.; Han, S. S.; Hong, C. S. *ChemSusChem* **2017**, *10* (3), 541.
(27) Lee, W. R.; Jo, H.; Yang, L.-M.; Lee, H.; Ryu, D. W.; Lim, K. S.; Song, J. H.; Min, D. Y.; Han, S. S.; Seo, J. G.; Park, Y. K.; Moon, D.; Hong, C. S. *Chem. Sci.* **2015**, *6* (7), 3697.
(28) Lee, W. R.; Hwang, S. Y.; Ryu, D. W.; Lim, K. S.; Han, S. S.; Moon, D.; Choi, J.; Hong, C. S. *Energy Environ. Sci.* **2014**, *7* (2), 744.
(29) Gygi, D.; Bloch, E. D.; Mason, J. A.; Hudson, M. R.; Gonzalez, M. I.; Siegelman, R. L.; Darwish, T. A.; Queen, W. L.; Brown, C. M.; Long, J. R. *Chem. Mater.* **2016**, *28* (4), 1128.
(30) Xiao, D. J.; Oktawiec, J.; Milner, P. J.; Long, J. R. *J. Am. Chem. Soc.* **2016**, *138* (43), 14371.
(31) Aubrey, M. L.; Long, J. R. *J. Am. Chem. Soc.* **2015**, *137* (42), 13594.
(32) Deng, H.; Grunder, S.; Cordova, K. E.; Valente, C.; Furukawa, H.; Hmadeh, M.; Gándara, F.; Whalley, A. C.; Liu, Z.; Asahina, S.; Kazumori, H.; O'Keeffe, M.; Terasaki, O.; Stoddart, J. F.; Yaghi, O. M. *Science* **2012**, *336* (6084), 1018.
(33) Ghysels, A.; Vanduyfhuys, L.; Vandichel, M.; Waroquier, M.; Van Speybroeck, V.; Smit, B. *J. Phys. Chem. C* **2013**, *117* (22), 11540.
(34) Castiglioni, E.; Biscarini, P.; Abbate, S. *Chirality* **2009**, *21* (1E), E28.
(35) MacMillan, D. W. C. *Nature* **2008**, *455* (7211), 304.
(36) Zhang, S.-Y.; Li, D.; Guo, D.; Zhang, H.; Shi, W.; Cheng, P.; Wojtas, L.; Zaworotko, M. J. *J. Am. Chem. Soc.* **2015**, *137* (49), 15406.
(37) Gutov, O. V.; Molina, S.; Escudero-Adán, E. C.; Shafir, A. *Chem. - Eur. J.* **2016**, *22* (38), 13582.
(38) Ebner, F.; Heller, A.; Rippke, F.; Tausch, I. *Am. J. Clin. Dermatol.* **2002**, *3* (6), 427.
(39) Stock, N.; Biswas, S. *Chem. Rev.* **2012**, *112* (2), 933.
(40) Hoffmann, H. C.; Paasch, S.; Muller, P.; Senkovska, I.; Padmanaban, M.; Glorius, F.; Kaskel, S.; Brunner, E. *Chem. Commun.* **2012**, *48* (85), 10484.
(41) Pickard, C. J.; Salager, E.; Pintacuda, G.; Elena, B.; Emsley, L. *J. Am. Chem. Soc.* **2007**, *129* (29), 8932.
(42) Salager, E.; Day, G. M.; Stein, R. S.; Pickard, C. J.; Elena, B.; Emsley, L. *J. Am. Chem. Soc.* **2010**, *132* (8), 2564.
(43) Bonhomme, C.; Gervais, C.; Babonneau, F.; Coelho, C.; Pourpoint, F.; Azaïs, T.; Ashbrook, S. E.; Griffin, J. M.; Yates, J. R.; Mauri, F.; Pickard, C. J. *Chem. Rev.* **2012**, *112* (11), 5733.
(44) Baias, M.; Widdifield, C. M.; Dumez, J.-N.; Thompson, H. P. G.; Cooper, T. G.; Salager, E.; Bassil, S.; Stein, R. S.; Lesage, A.; Day, G. M.; Emsley, L. *Phys. Chem. Chem. Phys.* **2013**, *15* (21), 8069.
(45) Baias, M.; Dumez, J.-N.; Svensson, P. H.; Schantz, S.; Day, G. M.; Emsley, L. *J. Am. Chem. Soc.* **2013**, *135* (46), 17501.
(46) Kieslich, G.; Forse, A. C.; Sun, S.; Butler, K. T.; Kumagai, S.; Wu, Y.; Warren, M. R.; Walsh, A.; Grey, C. P.; Cheetham, A. K. *Chem. Mater.* **2016**, *28* (1), 312.
(47) Flaig, R. W.; Osborn Popp, T. M.; Fracaroli, A. M.; Kapustin, E. A.; Kalmutzki, M. J.; Altamimi, R. M.; Fathieh, F.; Reimer, J. A.; Yaghi, O. M. *J. Am. Chem. Soc.* **2017**, *139* (35), 12125.
(48) Arunan, E.; Desiraju, G. R.; Klein, R. A.; Sadlej, J.; Scheiner, S.; Alkorta, I.; Clary, D. C.; Crabtree, R. H.; Dannenberg, J. J.; Hobza, P.; Kjaergaard, H. G.; Legon, A. C.; Mennucci, B.; Nesbitt, D. J. *Pure Appl. Chem.* **2011**, *83* (8), 1619.
(49) Clark, S. J.; Segall, M. D.; Pickard, C. J.; Hasnip, P. J.; Probert, M. I. J.; Refson, K.; Payne, M. C. *Z. Kristallogr. - Cryst. Mater.* **2009**, *220* (5/6), 567.
(50) Perdew, J. P.; Burke, K.; Ernzerhof, M. *Phys. Rev. Lett.* **1996**, *77* (18), 3865.
(51) Yates, J. R.; Pickard, C. J.; Mauri, F. *Phys. Rev. B: Condens. Matter Mater. Phys.* **2007**, *76* (2), 024401.
(52) Pickard, C. J.; Mauri, F. *Phys. Rev. B: Condens. Matter Mater. Phys.* **2001**, *63* (24), 245101.
(53) Griffin, J. M.; Berry, A. J.; Ashbrook, S. E. *Solid State Nucl. Magn. Reson.* **2011**, *40* (2), 91.
(54) Kim, G.; Griffin, J. M.; Blanc, F.; Haile, S. M.; Grey, C. P. *J. Am. Chem. Soc.* **2015**, *137* (11), 3867.
(55) Srebro-Hooper, M.; Autschbach, J. *Annu. Rev. Phys. Chem.* **2017**, *68* (1), 399.
(56) Autschbach, J. *Chirality* **2009**, *21* (1E), E116.

DOI: 10.1021/jacs.7b09983
J. Am. Chem. Soc. 2017, 139, 16000−16012